TRANSPARENT BOUNDARY CONDITIONS AS DISSIPATIVE SUBGRID CLOSURES FOR THE SPECTRAL REPRESENTATION OF SCALAR ADVECTION BY SHEAR FLOWS

MARCEL OLIVER AND OLIVER BÜHLER

ABSTRACT. We consider the evolution of a passive scalar in a shear flow in its representation as a system of lattice differential equations in wave number space. When the velocity field has small support, the interaction in wave number space is local and can be studied in terms of dispersive linear lattice waves. We close the restriction of the system to a finite set of wave numbers by implementing transparent boundary conditions for lattice waves. This closure is studied numerically in terms of energy dissipation rate and energy spectrum, both for a time-independent velocity field and for a time-dependent synthetic velocity field whose Fourier coefficients follow independent Ornstein–Uhlenbeck stochastic processes.

1. INTRODUCTION

Transport in fluid flow is often characterized by the presence of vastly different time and length scales. In particular, the simulation of most turbulent flows by direct numerical simulation, i.e., by solving a discrete version of the Navier–Stokes equations in a regime where *a priori* or *a posteriori* errors are small, is far beyond the reach of current computers. Computation of large scale features of such flows thus entails—explicitly or implicitly—the modeling of the impact of unresolved small scales on the scales of interest.

One such approach is *large eddy simulation* (LES), where a spatial filter is applied to the equation of motion. For a passive scalar θ advected by a divergence-free velocity field $\boldsymbol{u}$,

$$\partial_t \theta + \boldsymbol{u} \cdot \boldsymbol{\nabla} \theta = 0 \,, \tag{1}$$

define filtered fields $\overline{\theta} = G * \theta$ and $\overline{\boldsymbol{u}} = G * \boldsymbol{u}$ through convolution with a suitable mollifier G. Since multiplication and mollification do not commute, the filtered equation reads

$$\partial_t \overline{\theta} + \overline{\boldsymbol{u}} \cdot \boldsymbol{\nabla} \overline{\theta} = \overline{\boldsymbol{u}} \cdot \boldsymbol{\nabla} \overline{\theta} - \overline{\boldsymbol{u} \cdot \boldsymbol{\nabla} \theta} \equiv \boldsymbol{\nabla} \cdot \boldsymbol{\tau} \,, \tag{2}$$

where $\boldsymbol{\tau}$ is called the *subgrid stress*. Equation (2) is obviously not closed; the art of LES modeling consists in expressing $\boldsymbol{\tau}$ in terms of $\overline{\theta}$ and $\overline{\boldsymbol{u}}$ such that, on the one hand, important structural and statistical properties are maintained and, on the other hand, the model is stable for computation on a coarse grid. Such closures—either as above for the advection equation or, similarly, for the full equations of fluid motion—are not approximations in the strict mathematical sense. They typically lack a precise notion of metric, of small parameter, and thus of convergence, but there is a vast body of experience through numerical and experimental validation with different LES closures; see, e.g., the review by Meneveau and Katz [14]. Even

Date: January 7, 2007.

though LES is often highly successful in simulation, the abstract "closure problem" is still far from solved; indeed, a universal closure scheme cannot be expected because any successful closure scheme must exploit a specific physical feature of the flow under consideration, which makes closure schemes problem-dependent.

In this work, we address a very special case of the closure problem where a systematic subgrid model can be derived: the case when the support, in wave number space, of the advecting velocity is small compared to the cut-off wavenumber of the filter.[1]Physically, this corresponds to the Batchelor regime of passive advection, in which the advecting velocity has much larger scale than the advected field. This situation is very different from fully developed three-dimensional turbulence, where advected and advecting fields coincide and possess features beyond the grid scale. On the other hand, many flows of practical importance do fall into this category. Stirring at large scales can induce chaotic mixing as exemplified by the ABC flow [7]; instances of such mixing flows abound in engineering.

Another important example is that of large-scale flows in geophysical fluid dynamics. Typically, large-scale flows in the atmosphere and oceans are dominated by layerwise quasi-two-dimensional motion along density stratification surfaces. Mutatis mutandis, such flows are subject to the basic phenomenology of two-dimensional turbulence with the attendant inverse cascade of kinetic energy towards large scales; see, for example, [16]. This inverse cascade makes the Batchelor regime directly relevant for tracer advection in geophysical flows [11].

Furthermore, large-scale geophysical flows are approximately governed by the three-dimensional distributions of an active scalar tracer called the *potential vorticity* (PV); see [16]. The large-scale velocity field can be approximately computed by convolving the PV with a smoothing kernel, which implies that the advecting velocity field is smoother than the advected PV field. This makes our approach relevant to active tracers such as PV as well. However, in the present paper we restrict ourselves to passive tracers.

When the advecting velocity field $\boldsymbol{u}$ has only very large scales, i.e., when its support in wave number space is restricted to a small fraction of the numerically resolvable scales, advection can be thought of acting locally in wave number space. This locality of the interaction permits an analysis in terms of dispersive linear lattice waves as are classical in solid state physics [3, 4] and have also been used in the analysis of finite difference schemes for hyperbolic PDEs [20, 18, 22, 9].

The simplest truncation to a finite set of wave numbers is the Galerkin projection onto the set of Fourier modes with wave numbers $|\boldsymbol{k}| \leq N$. The Galerkin-truncated system is conservative. Correspondingly, in the lattice wave picture, we find that waves are reflected at the cut-off boundary, thereby polluting the modes below the cut-off and, in particular, altering the tracer energy (or variance) spectrum. To avoid such reflections, we must implement nonreflecting boundary conditions in wave number space which allow energy to move out of the resolved range without being reflected.

Non-reflecting boundary conditions for linear advection and advection-diffusion equations in physical space have a long history and are, by now, well understood [10, 12, 5, 15]. Here, we generalize the approach of Colonius [5] and Rowley and

[1]Other assumptions about the advecting velocity field lead to other systematic closure schemes; e.g., in the Kraichnan model for stochastic velocity fields substantial progress can be made (see [1] and references therein).

Colonius [15], based on earlier work of Vichnevetsky and co-workers [20, 22], to allow dynamic computation of the nonreflecting boundary condition for complex dispersion relations, and implement these boundary conditions in wave number space.

Two remarks are in order. First, this situation is different from studying fully developed turbulence, where the best one can hope for is correctness in the statistical sense and where closure means, above all, implementing correct time-averaged energy fluxes. Second, the connection between non-reflecting boundary conditions and LES closure is not new—Colonius and Ran [6], driven by the observation that for fully nonlinear flow problems none of the established methods, all based on linear wave theory, works unconditionally well, set out to derive nonlinear non-reflecting boundary conditions by using an LES-like closure in wave number space. This is the dual point of view of what we propose here, and of what is normally done.

In the present paper, we focus on shear flows in two dimensions where the closure problem reduces to a computation on a one-dimensional lattice. The general case is subject to a forthcoming paper. Specifically, we consider the advection equation

$$\partial_t \theta + \boldsymbol{u} \cdot \boldsymbol{\nabla} \theta = 0 \tag{3}$$

on the doubly periodic domain $\mathbb{T}^2 \equiv [-\pi, \pi]^2$ with a velocity field

$$\boldsymbol{u}(\boldsymbol{x}, t) = \begin{pmatrix} u(y,t) \\ 0 \end{pmatrix} . \tag{4}$$

This simple shear flow example has the exact solution

$$\theta(x, y, t) = \theta\left(x - \int_0^t u(y,t)\,\mathrm{d}t, y, 0 \right), \tag{5}$$

which is characteristic for sheared-over disturbances and exhibits the secular development of fine y-scales. In the Fourier representation, equation (3) reads

$$\partial_t \theta_{kl} + \mathrm{i}k \sum_{m+n=l} u_m\, \theta_{kn} = 0\,, \tag{6}$$

where we take the convention

$$f_k = \frac{1}{2\pi} \int_{-\pi}^{+\pi} \mathrm{e}^{-\mathrm{i}kx}\, f(x)\,\mathrm{d}x \tag{7}$$

for the Fourier transform in one dimension.

Equation (6) exhibits the basic closure problem in spectral space because the Fourier modes of θ are coupled to neighboring modes over a range of wavenumbers proportional to the radius of spectral support of the u. In a numerical simulation with a finite number of modes (6) must be truncated in some way near the boundary of the spectral grid. At first sight, the usual Galerkin projection appears attractive because it maintains a discrete version of the integral conservation law for the variance θ^2. However, this conservation law is precisely what one does *not* wish to see in a faithful simulation of the advection equation truncated to a finite spectral domain. Instead, the variance of θ associated with a finite wavenumber domain should *decrease* due to the flux of θ^2 across the boundary of the spectral grid.

In practice, this variance-diminishing flux is often modeled by adding a scale-selective artificial diffusion term on the right-hand side of (3). A common choice in spectral schemes is the 'hyperdiffusion' (or 'hyperviscosity' in the geophysical literature) term $\nu\,(-1)^{p-1}\nabla^{2p}\theta$ of order $2p$. Here $p \geq 1$ is an integer and $p = 4$

is a typical choice. In essence, this artificial diffusion acts as a damping layer near the boundary of the spectral grid and as such it approximates a non-reflecting boundary condition. One problem with this approach is how to tune the resolution-dependent coefficient ν. For instance, it is well known that in forced–dissipative simulations of statistically steady states the chosen value of ν can affect the energy spectrum over a large range of wavenumbers and not just near the cut-off. This gives rise to subtle controversies over the nature of observed and simulated spectral characteristics [19, 17].

In this paper we pursue a different idea, namely whether the spectral truncation of the advection equation can be modeled by a non-reflecting boundary condition for the waves on the spectral lattice defined by (6). The paper is organized as follows. We first review the Vichnevetsky–Colonius approximate nonreflecting numerical boundary conditions and reformulate their algorithm in a framework that is more amenable to generalization. In Section 4 we introduce our general setting, explain several variants of the algorithm, derive the energy dissipation rate for closures of this type and define generalized reflection coefficients which are based on the error in the energy dissipation rate. The various closures are numerically tested and compared in the following Section 5. Our synthetic time-dependent velocity fields are based on simple Ornstein–Uhlenbeck stochastic processes. In Section 6, we modify the lattice wave picture to account for dispersion curves with such time-dependent coefficients. These ideas are numerically validated in the final Section 7.

So far, we have chosen a a simple, quasi-onedimensional setting—shear flows where the shearing velocity field is supported on only a few largest-scale modes in the Fourier domain. In principle, similar closures can be used in higher dimensions which, however, are complicated by the fact that the normal modes used in the analysis of Section 3 cease to be exact solutions of the system of lattice ODEs. Moreover, a quantitative validation of such nonreflecting closures in the case where the velocity field has unbounded support in Fourier space, but its coefficients decay at a rapid, specified rate, is of particular importance for active PV advection. Both problems will be addressed in forthcoming work.

2. Setup

Throughout the paper, we work in the following setting. In the Fourier representation of advection by a shear flow, the horizontal wave number k acts as a parameter, so that the only dynamically relevant index is the vertical wave number l. We thus drop the k-subscript and write (6) in the form

$$\dot{\theta}_l = \sum_{j=-M}^{M} c_j \, \theta_{l-j} \tag{8}$$

where

$$c_j = -\mathrm{i}k u_j \, . \tag{9}$$

Since u is real, $u_{-j} = \overline{u}_j$ and therefore

$$c_{-j} = -\overline{c}_j \, . \tag{10}$$

Moreover, we assume that there is no overall drift, so that $c_0 = 0$.

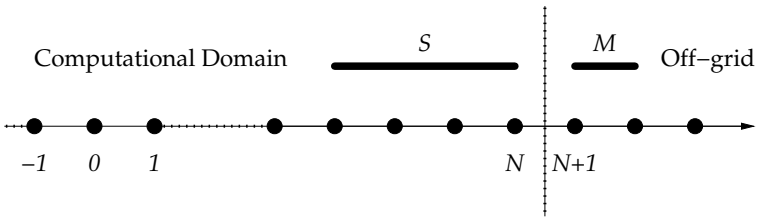

FIGURE 1. Sketch of right lattice boundary.

2.1. **Group velocity.** The behavior of (8) is best understood in terms of dispersive lattice waves. The concept of *group velocity*, the velocity at which energy (or variance) is traveling along the lattice, is of central importance. We give a brief motivation, following the stationary phase argument as used in [18].

We look for normal mode solutions of the form

$$\theta_l = \mathrm{e}^{\mathrm{i}\omega t - \mathrm{i}l\xi} \equiv \mathrm{e}^{\mathrm{i}\omega t}\,\kappa^l \tag{11}$$

where $\kappa = \kappa(\xi) = \exp(-\mathrm{i}\xi)$. Substitution into (8) leads to the *dispersion relation*

$$\omega(\xi) = -\mathrm{i}\sum_{j=-M}^{M} c_j\,\kappa^{-j}\,. \tag{12}$$

Note that $\omega(\xi) = -k\,u(\xi)$; in other words, the dispersion curve is nothing but the shear profile. The solution to (8) is then given by the Fourier integral

$$\theta_l(t) = \frac{1}{2\pi}\int_{-\pi}^{\pi} \mathrm{e}^{\mathrm{i}l(\omega(\xi)t/l - \xi)}\,\theta(\xi,0)\,\mathrm{d}\xi\,. \tag{13}$$

When l is large, the exponential factor oscillates rapidly, unless

$$\frac{\mathrm{d}}{\mathrm{d}\xi}\left(\omega(\xi)\frac{t}{l} - \xi\right) = 0\,. \tag{14}$$

In other words, if we track the solution along a line moving with the *group velocity* $l/t = \omega'(\xi)$, we see only waves of wavenumber ξ as $t, l \to \infty$.

2.2. **Closure conditions.** In a computational setting, the resolvable wavenumbers will be restricted to a finite range $|l| \le N$. Thus, the differential equation (8) couples the highest represented mode θ_N to M off-grid nodes $\theta_{N+1}, \ldots, \theta_{N+M}$. To specify the values for these quantities, we seek a linear map $A\colon \mathbb{R}^S \to \mathbb{R}^M$ between the rightmost S on-grid nodes to the leftmost M off-grid nodes, see Figure 1, so that

$$\begin{pmatrix} \theta_{N+1} \\ \vdots \\ \theta_{N+M} \end{pmatrix} = A \begin{pmatrix} \theta_{N-S+1} \\ \vdots \\ \theta_N \end{pmatrix}\,. \tag{15}$$

The matrix A shall be determined such that outgoing waves, i.e. normal mode solutions (11) with positive group velocity, will be left as undisturbed as possible, in other words, that reflections of outgoing to incoming waves will be minimized. The situation at the left boundary $l = -N$ is symmetrical.

3. Colonius' discretely nonreflecting boundary conditions

In the following, we discuss several ways of computing a suitable closure map A. We first review the derivation of Colonius [5], further discussed and extended to several dimensions in Rowley and Colonius [15]. Our goal is to cast this procedure into a different, but equivalent framework which is more amenable to generalization.

Essentially, the Colonius closure scheme is based on controlling the outgoing waves in the neighbourhood of the zero-frequency roots $\omega(\xi) = 0$ of the dispersion relation. This is natural in the finite-difference application studied in [5] because in this application $\omega \to 0$ as the grid spacing $h \to 0$. In our case, there is nothing special about zero-frequency roots, which in physical space correspond to locations $y = \xi$ at which the shear flow $u = -\omega/k = 0$. However, the Colonius scheme can easily be generalized and therefore used as a starting point.

A few further remarks are in order. First, lattice ODEs of the form (8) are not precisely the system that Colonius worked with. We, on the one hand, consider stencils of arbitrary size from the outset. Colonius, on the other hand, permits linear couplings between neighboring time derivatives on the left hand side of (8); in our situation there is no need for doing so, but there is also no fundamental obstacle to including systems of this type into our framework.

Second, in [5] the relation $\omega(0) = 0$ always held due to consistency requirements. Thus, the limit $h \to 0$ corresponds to $\xi \to 0$, so that lattice waves near $\xi = 0$ are of particular interest. Our situation is completely different: ξ corresponds to physical space so that there is nothing special about $\xi = 0$; moreover, the lattice spacing relates to the physical domain size and therefore is not small. These differences require modifications which are discussed in Section 4.

Third, as far as the boundary conditions go, there is nothing special about $l = N$. Therefore, we translate the computations on the lattice to a location which allows for the most convenient indexing. The assumption that $N \gg M$ is nonetheless important in that it guarantees that we are close to the stationary phase limit in the solution integral (13). Only in this limit do lattice waves provide a good description of the true dynamics.

The basic idea is that the boundary condition is determined by the condition that the vector

$$\Theta = (\theta_1, \dots, \theta_S, \theta_{S+1}, \dots, \theta_{S+M}) \tag{16}$$

(where, without loss of generality, we have fixed the boundary at $N = S$) lies in a certain subspace that characterizes outgoing waves. In the following, we characterize this subspace as the kernel of a certain linear map.

3.1. Boundary condition for $M = 1$.

For $M = 1$ the shear flow has simple a sinusoidal profile, i.e. modulo translation and scaling, $u(\xi) = -\sin\xi$, and the lattice equations can be solved explicitly (see Appendix A), which allows easy comparison with the closure scheme. The corresponding dispersion relation $\omega = -ku = k\sin\xi$ has two distinct zero-frequency roots at $\xi_{1,2} = \{0, \pi\}$, say. The first root corresponds to a wave with positive group velocity, the second to a wave with negative group velocity. Let us consider the right lattice boundary, where the root with positive group velocity, in the following denoted by $\kappa_1 = \exp(-i\xi_1)$, corresponds to an outgoing, hence physical wave, and the root with negative group velocity corresponds to an incoming, hence spurious wave.

For a given boundary stencil of size S, let $Q \equiv S$ denote the order of the scheme in the terminology of [5]. Then

$$\Theta(\kappa) = \mathrm{e}^{\mathrm{i}\omega t}\,(1, \kappa, \ldots, \kappa^Q) \tag{17}$$

denote $Q+1$ consecutive samples of a normal mode (11). The sample nodes correspond to a boundary stencil of size S plus the $M = 1$ off-grid node required to close the system.

Since we want to optimally characterize outgoing waves near the root $\kappa = \kappa_1$, we seek a linear functional $\ell(\Theta)$ that not only annihilates (17), but also its first $Q-1$ derivatives with respect to ω. In other words, we require that

$$\left.\frac{\mathrm{d}^j \ell(\Theta)}{\mathrm{d}\omega^j}\right|_{\omega=0} = 0 \qquad \text{for } j = 0, \ldots, Q-1 \tag{18}$$

where the differentiation with respect to ω is carried out implicitly with the understanding that the inversion is near the root $\kappa = \kappa_1$ which corresponds to the outgoing wave. In the case of finite difference schemes, where ω is scaled with the spatial stepsize h, (18) implies that the resulting reflection coefficients go to zero with order Q as $h \to 0$ [21, 5]. Note, however, that a small parameter of this kind is not available in our setting.

For actual computation, it is easier to express (18) directly in terms of κ derivatives. Indeed, through successive implicit differentiation, we find the equivalent condition

$$\left.\frac{\mathrm{d}^j \ell(\Theta)}{\mathrm{d}\kappa^j}\right|_{\kappa=\kappa_1} = 0 \qquad \text{for } j = 0, \ldots, Q-1\,. \tag{19}$$

When the order condition is written this way, it is easy to see that

$$\ell(\Theta) = \sum_{k=0}^{Q} \binom{Q}{k} (-\kappa_1)^k\, \theta_{Q-k} \tag{20}$$

possesses property (18) since, by (11) and the binomial theorem, the sum on the right equals

$$\mathrm{e}^{\mathrm{i}\omega t} \sum_{k=0}^{Q} \binom{Q}{k} (-\kappa_1)^k\, \kappa^{Q-k} = \mathrm{e}^{\mathrm{i}\omega t}\,(\kappa - \kappa_1)^Q\,. \tag{21}$$

The approximate nonreflecting boundary condition is now obtained by solving $\ell(\Theta) = 0$ for the single off-grid node θ_Q. Substituting this relationship back into (8) yields the same ODE for the boundary node θ_{Q-1} as stated in [5].

Remark 1. The error committed by the extrapolation identity (20) can be assessed in terms of the closed form solution (76) as follows. Recall the recurrence identity for Bessel functions [2, 9.1.27],

$$J_{l-1}(t) - 2\,\frac{l}{t}\,J_l(t) + J_{l+1}(t) = 0\,. \tag{22}$$

In the cases considered in [5], the dispersion curve always passes the origin, so that $\kappa_1 = 1$. Consequently, the recurrence identity (22) for the exact solution coincides with the closure condition $\ell(\Theta) = 0$ for $Q = 2$ in the limit $l/t \to 1$. This corresponds to following the wave packet with maximal group velocity. For other values of Q, we can compute a "consistency error" by plugging the exact solution (76) into $\ell(\Theta)$.

For exact closure, the expression should vanish, so the magnitude of the remainder can be used to quantify the error. In particular, for $Q = 0$, we obtain

$$J_l(l) = O(l^{-1/3}) \qquad \text{as } l \to \infty \tag{23}$$

and for $Q = 1$,

$$J_l(l) - J_{l+1}(l) = J_l'(l) = O(l^{-2/3}) \qquad \text{as } l \to \infty\,, \tag{24}$$

see [2, 9.3.31/33]. For $Q > 2$, the error committed when plugging (76) into (20) can be expressed, after using Bessel function recurrence identities, in terms of (23), (24), and $1 - l/t$. Hence, the analysis of this error involves the interplay of the two limits $l \to \infty$ and $l/t \to 1$.

Remark 2. We can also derive (20) from a different point of view. Condition (19) implies that the coefficient vector of ℓ spans the one-dimensional kernel of the $Q \times (Q+1)$ matrix

$$B(\kappa_1) \equiv \begin{pmatrix} \kappa_1^0 & \kappa_1^1 & \kappa_1^2 & \cdots & \kappa_1^Q \\ 0 & \kappa_1^1 & 2\,\kappa_1^2 & \cdots & Q\kappa_1^Q \\ 0 & \kappa_1^1 & 4\,\kappa_1^2 & \cdots & Q^2\kappa_1^Q \\ \vdots & \vdots & \vdots & & \vdots \\ 0 & \kappa_1^1 & 2^{Q-1}\,\kappa_1^2 & \cdots & Q^{Q-1}\kappa_1^Q \end{pmatrix}. \tag{25}$$

Thus, (20) can be derived by direct Gauss elimination. This ansatz is particularly amenable to automated computation of the boundary operators and can easily be generalized to the case when $M > 1$.

Remark 3. It is straightforward to generalize the above ideas to the case when the boundary operator involves derivatives at different grid nodes and higher order time derivatives as in some of the closures proposed by Colonius [5].

3.2. **Boundary condition for $M \geq 2$.** In general, we must relate the M nodes that lie outside of the boundary to S nodes within the domain. Counting multiplicities, the dispersion relation now has $2M$ distinct zeros, which we label $\kappa_1, \ldots, \kappa_{2M}$. These roots have to be classified according to whether they correspond to spurious or physical waves. There are two cases: the roots where κ is on the unit circle in the complex plane, corresponding to real values of ξ, and those where $|\kappa| \neq 1$, corresponding to a nonzero imaginary part of ξ. While the former represent unattenuated waves, the latter have exponential growth or decay in l, and are called evanescent waves. If the roots are distinct, there are exactly M spurious and M physical waves. A wave corresponding to a unit root is physical if its group velocity is pointing out of the boundary and spurious if its group velocity is pointing into the boundary. An evanescent wave is spurious if it is increasing toward the boundary, and physical if it is decreasing toward the boundary.

Remark 4. Our assumptions on the c_l restrict the patterns of roots that can occur. First, $\kappa = \pm 1$ is necessarily a pair of roots. If κ is a root, then κ^{-1} is also a root. Finally, if κ is a root, then $\overline{\kappa}$ is also a root.

Remark 5. Pairs of roots on the unit circle are structurally stable with respect to small perturbations of the coefficients, as they have to either pass through ± 1 or "collide" with another pair of unit roots in order to get off the unit circle.

Remark 6. In our case, the initial data do not contain evanescent waves. Since traveling waves do not reflect into evanescent waves, we can set up our extrapolation operators to extrapolate traveling waves only. Since, for a fixed sized stencil, this allows for better extrapolation of traveling waves, we will do so in the remainder of this paper.

If we want to find a closure of the same fixed order Q near each of the roots, then we must take a boundary stencil of size $S = MQ$ and need the corresponding number of equations to specify the boundary condition uniquely. In other words, we are looking for a linear map $L\colon \mathbb{R}^{S+M} \to \mathbb{R}^M$ which satisfies condition (19) at each of the roots of the dispersion relation that correspond to outgoing lattice waves. When $M \geq 2$, there is no obvious way of finding a closed form expression for L, but we can easily generalize the linear algebra of the $M = 1$ case.

Let $\kappa_1, \ldots, \kappa_M$ denote the physical waves at the chosen boundary. Then L is the $(S + M) \times M$ matrix with linearly independent columns which satisfies

$$\begin{pmatrix} B(\kappa_1) \\ B(\kappa_2) \\ \vdots \\ B(\kappa_M) \end{pmatrix} L = 0\,, \tag{26}$$

where each $B(\kappa_i)$ is a $Q \times (S + M)$ block of the form (25). When this equation is solved by standard Gauss elimination, L emerges naturally in the form

$$L = \begin{pmatrix} A^T \\ -I \end{pmatrix} \tag{27}$$

where A is the $M \times S$ matrix featuring in the boundary closure (15).

3.3. **Example.** As an example, we consider the case $M = 2$ with $c_{-2} = 1/2$, $c_{-1} = c_0 = c_1 = 0$, and $c_2 = -1/2$. Thus, we have two uncoupled, interleaved systems of the form (71). The dispersion relation reads

$$\omega = \sin 2\xi \tag{28}$$

on the fundamental domain $\xi \in (-\pi, \pi]$. The roots are at $-\pi/2$, 0, $\pi/2$, and π; we consider the right boundary so that we need to select the roots corresponding to a positive group velocity, which are $\xi = 0$ and $\xi = \pi$ corresponding to $\kappa_1 = 1$ and $\kappa_2 = -1$. We choose the simplest nontrivial case, $Q = 2$, and must therefore solve

$$\begin{pmatrix} 1 & 1 & 1 & 1 & 1 & 1 \\ 0 & 1 & 2 & 3 & 4 & 5 \\ 1 & -1 & 1 & -1 & 1 & -1 \\ 0 & -1 & 2 & -3 & 4 & -5 \end{pmatrix} L = 0\,, \tag{29}$$

the solution to which is readily computed as

$$L^T = \begin{pmatrix} -1 & 0 & 2 & 0 & -1 & 0 \\ 0 & -1 & 0 & 2 & 0 & -1 \end{pmatrix}, \tag{30}$$

so that, as expected, the boundary condition decouples into two interleaved Colonius-type order 2 closures.

4. General nonreflecting boundary conditions

4.1. **Setup.** We observe that our lattice ODE does not have a built-in spatial step-size scaling; thus, we are not in a situation where a (rescaled) ω can be considered small. Consequently, we must sample the dispersion relation at a more general set of lattice wave numbers ξ. In physical space, this corresponds to sampling the shear flow $u = -\omega/k$ at more than one location $y = \xi$. We consider, for ease of notation, the case of the right hand boundary only, and fix S sample wavenumbers $\xi_1, \dots, \xi_S$ which correspond to outgoing, here rightgoing, waves. As before, $\kappa_j = \exp(-\mathrm{i}\xi_j)$ denote the corresponding multipliers.

At each of these sample modes, we require an order $Q = 1$ closure condition, i.e., we require that the suitable linear functionals annihilate the relevant $S + M$ function values that correspond to outgoing normal modes. The matrix whose row space is the set of chosen modes, analogous to the left hand matrix in (26), then reads

$$(B, C) = \begin{pmatrix} \kappa_1^1 & \dots & \kappa_1^S & \kappa_1^{S+1} & \dots & \kappa_1^{S+M} \\ \vdots & & \vdots & \vdots & & \vdots \\ \kappa_S^1 & \dots & \kappa_S^S & \kappa_S^{S+1} & \dots & \kappa_S^{S+M} \end{pmatrix}, \tag{31}$$

which we separate into blocks $B \in \mathbb{R}^{S\times S}$ and $C \in \mathbb{R}^{S\times M}$; we assume that B is nonsingular. The row space of (B, C) is invariant with respect to left multiplication by a nonsingular matrix and, hence, is also spanned by $(I, B^{-1}C)$. Thus, the nonreflecting boundary condition is

$$\begin{pmatrix} \theta_{S+1} \\ \vdots \\ \theta_{S+M} \end{pmatrix} = (B^{-1}C)^T \begin{pmatrix} \theta_1 \\ \vdots \\ \theta_S \end{pmatrix}, \tag{32}$$

where $\theta_1, \dots, \theta_S$ are grid values within the lattice domain, and $\theta_{S+1}, \dots, \theta_{S+M}$ the virtual grid points outside the domain of computation which are necessary to close the lattice ODE.

There is no *a priori* best choice of sample wave numbers $\xi_1, \dots, \xi_S$. Before discussing strategies for choosing the sample modes in our setting, we remark that a closure of order $Q > 1$ at a certain wavenumber ξ can be obtained via the above procedure by taking $\xi, \xi + h, \dots, \xi + (Q-1)\,h$ among the sample wavenumbers, then letting $h \to 0$. Thus, there is no need to explicitly consider higher order closures.

4.2. **Equidistant sampling.** When the velocity field (and correspondingly, the dispersion relation) is smooth, equidistant sampling is an obvious choice. Equidistant sampling is easy to implement and guarantees a well-conditioned matrix inversion in (32).

We adopt the following notation. Let S^{smpl} denote the number of sample wave numbers and set $h = 2\pi/S^{\mathrm{smpl}}$. We then sample the dispersion relation, for example, at wave numbers

$$\xi_j = -\pi + jh \qquad \text{for } j = 1, \dots, S^{\mathrm{smpl}}. \tag{33}$$

The modes are then sorted into right and leftgoing waves according to the sign of their group velocity. At the right boundary, only rightgoing sample modes are physical and can be used to span the subspace in which to extrapolate. Generally, we will have $S^{\mathrm{out}} \le S^{\mathrm{smpl}}$ outgoing modes which we label $\xi_{r(j)}$ with corresponding multipliers $\kappa_{r(j)} = \exp(-\mathrm{i}\xi_{r(j)})$ for $j = 1, \dots, S^{\mathrm{out}}$. A natural choice is to let

$S = S^{\text{out}}$, i.e. the size of the boundary stencil equals the number of available equations, so that matrix (31) takes the form

$$(B, C) = \begin{pmatrix} \kappa_{r(1)}^1 & \dots & \kappa_{r(1)}^S & \kappa_{r(1)}^{S+1} & \dots & \kappa_{r(1)}^{S+M} \\ \vdots & & \vdots & \vdots & & \vdots \\ \kappa_{r(S)}^1 & \dots & \kappa_{r(S)}^S & \kappa_{r(S)}^{S+1} & \dots & \kappa_{r(S)}^{S+M} \end{pmatrix} . \tag{34}$$

The nonreflecting boundary condition is again given by (32).

4.3. **Least-norm solution.** Equidistant sampling has two drawbacks. First, the size of the boundary stencil at each boundary depends on the dispersion curve. As such, it is not something we could easily control. Second, when the velocity field is a smooth function of time, the extrapolation operators, depending only on the partition of the sample modes into left- and right-going waves, are discontinuous in t. This can, in particular, cause problems for the step size control of the time integrator. These problems can be overcome, on the expense of increasing the size of the linear system (34), by oversampling the dispersion curve. The resulting system for the coefficients of the extrapolation is then underdetermined and needs to be solved in a least-norm sense.

We fix the size of the boundary stencil S and, independently, the number of sample points S^{smpl}. As we demonstrate numerically in Section 5, the quality of the extrapolation depends very little on S^{smpl}. Hence, S^{smpl} should be chosen such that, on the one hand, it is large enough so that for every dispersion curve under consideration there are at least S samples of waves in each direction. On the other hand, S^{smpl} should not be too much larger for computational efficiency.

We begin by noting that the direct solution to the closure problem, equation (32), can be formulated as follows. *Solve*

$$B^T z = \begin{pmatrix} \theta_1 \\ \vdots \\ \theta_S \end{pmatrix} , \tag{35}$$

then set

$$\begin{pmatrix} \theta_{S+1} \\ \vdots \\ \theta_{S+M} \end{pmatrix} = C^T z \, . \tag{36}$$

Here, however, we do not have an invertible B-matrix. All we can say is that, at the right boundary, there are $S^{\text{out}} < S^{\text{smpl}}$ outgoing modes which we label $\xi_{r(j)}$ with corresponding multipliers $\kappa_{r(j)} = \exp(-\mathrm{i}\xi_{r(j)})$ for $j = 1, \dots, S^{\text{out}}$. In general, $S \le S^{\text{out}}$, so that the B-block in (31) has more rows than columns; we write

$$(B, C) = \begin{pmatrix} \kappa_{r(1)}^1 & \dots & \kappa_{r(1)}^S & \kappa_{r(1)}^{S+1} & \dots & \kappa_{r(1)}^{S+M} \\ \vdots & & \vdots & \vdots & & \vdots \\ \kappa_{r(S^{\text{out}})}^1 & \dots & \kappa_{r(S^{\text{out}})}^S & \kappa_{r(S^{\text{out}})}^{S+1} & \dots & \kappa_{r(S^{\text{out}})}^{S+M} \end{pmatrix} . \tag{37}$$

Our least-norm problem then is the following. *Minimize*

$$\|z\|_W^2 = z^H W z \tag{38}$$

subject to (35)*, then set* (36). The positive definite weight matrix W is useful if we want to preserve continuity of the resulting extrapolation operator when a sample

wave crosses over from being rightgoing to being leftgoing, or vice versa, in the time-dependent case. To this end, we choose

$$W = \operatorname{diag}\left(|\omega'(\xi_{r(1)})|^{-1}, \dots, |\omega'(\xi_{r(S^{\text{out}})})|^{-1}\right) , \tag{39}$$

so that slow waves are most heavily penalized against. It is known that the solution to this least-norm problem can be computed via the QR-decomposition

$$QR = W^{-1/2}B\,, \tag{40}$$

where the least-norm solution is given by

$$z = W^{-1/2}\,\overline{Q}\,R^{-T}\begin{pmatrix}\theta_1\\ \vdots \\ \theta_S\end{pmatrix} \tag{41}$$

and the resulting boundary condition reads

$$\begin{pmatrix}\theta_{S+1}\\ \vdots \\ \theta_{S+M}\end{pmatrix} = (R^{-1}Q^H W^{-1/2}C)^T \begin{pmatrix}\theta_1\\ \vdots \\ \theta_S\end{pmatrix} . \tag{42}$$

Note that, although the definition of the weights may be singular, the resulting QR-decomposition (40) and the final extrapolation operator in (42) are not.

4.4. **Other choices.** If high accuracy over short times is required, it is best to concentrate the sample points near the maxima of the group velocity. Such closures behave like the Colonius-type closures of Section 3 (often, as in the cases considered in [5], the roots of the dispersion relation coincide with the maxima of the group velocity). However, they have larger long-time energy errors and are more difficult to implement as compared to equidistant sampling.

In general, our nonreflecting boundary conditions (32) require the inversion of a matrix or, in the least-norm setting, a QR-decomposition. If efficiency of this inversion is an issue, there is the following computationally cheap alternative. Instead of oversampling the dispersion relation, we may undersample equidistantly, taking $S = S^{\text{smpl}}$.

$$U = \begin{pmatrix}\kappa_1^1 & \dots & \kappa_1^S\\ \vdots & & \vdots \\ \kappa_S^1 & \dots & \kappa_S^S\end{pmatrix} \tag{43}$$

is then (a multiple of) a unitary matrix. (In fact, it is the matrix of the discrete Fourier transform.) The matrix B as analogous to (37) is then obtained from U by deletion of all rows which correspond to leftgoing waves. Hence, the rows of B are orthogonal and the pseudoinverse of B is B^H/S^{smpl}. This pseudoinverse is then used in the nonreflecting boundary condition (32), which is equivalent to projecting the vector of grid values $(\theta_{N-S+1}, \dots, \theta_N)$ onto the select set of outgoing modes, then extrapolating these modes onto their off-grid values. In our situation, the undersampled closure has, for a stencil of given size, reflections that are much stronger as compared to using the optimal stencil $S = S^{\text{out}}$. We might be tempted to compensate for this by further increasing the size of the boundary stencil as the computations are cheap. This, however, takes us farther away from the stationary phase limit in (13), hence increasing an independent source of error.

4.5. **Energy equation.** We consider the ℓ^2 energy on the half lattice $j \le S$,

$$E = \sum_{j \le S} |\theta_j|^2 \,. \tag{44}$$

By direct computation,

$$\begin{aligned}
\frac{\mathrm{d}E}{\mathrm{d}t} &= 2\ \mathrm{Re} \sum_{j \le S} \theta_j \sum_{l=-M}^{M} c_l\, \overline{\theta}_{j+l} \\
&= 2\ \mathrm{Re} \left[\sum_{l=1}^{M} c_l \sum_{j \le S} \theta_j\, \overline{\theta}_{j+l} - \sum_{l=1}^{M} c_l \sum_{j \le S-l} \theta_{j+l}\, \overline{\theta}_j \right] \\
&= 2\ \mathrm{Re} \sum_{l=1}^{M} c_l \sum_{j=1}^{l} \theta_{S+j-l}\, \overline{\theta}_{S+j}
\end{aligned} \tag{45}$$

provided that $\theta_k \to 0$ as $k \to -\infty$. Assuming a boundary closure of the form

$$\theta_{S+j} = \sum_{m=1}^{S} a_{j,m}\, \theta_m \tag{46}$$

for $j = 1, \dots, M$, we obtain

$$\begin{aligned}
\frac{\mathrm{d}E}{\mathrm{d}t} &= 2\ \mathrm{Re} \sum_{l=1}^{M} c_l \sum_{j=1}^{l} \theta_{S+j-l} \sum_{m=1}^{S} a_{j,m}\, \overline{\theta}_m \\
&= 2\ \mathrm{Re} \sum_{l=1}^{M} c_l \sum_{n=S+1-l}^{S} \theta_n \sum_{m=1}^{S} a_{n+l-S,m}\, \overline{\theta}_m \\
&= 2\ \mathrm{Re} \sum_{m,n=S_0}^{S} \theta_n\, \overline{\theta}_m \sum_{l=S+1-n}^{M} c_l\, a_{n+l-S,m} \,,
\end{aligned} \tag{47}$$

where $S_0 = \min\{1, S - M + 1\}$ and $a_{n,m} \equiv 0$ for $m \le 0$.

A similar computation on the half-lattice $j > M$ yields an equation for the energy transfer through a left boundary with linear closure

$$\theta_j = \sum_{m=1}^{S} a_{j,m}\, \theta_{M+m} \,, \tag{48}$$

namely

$$\frac{\mathrm{d}E}{\mathrm{d}t} = 2\ \mathrm{Re} \sum_{m,n=0}^{S_1} \theta_{M+n}\, \overline{\theta}_{M+m} \sum_{l=n}^{M} c_l\, a_{M+n-l,m} \,, \tag{49}$$

where $S_1 = \max\{M, S\}$ and $a_{n,m} \equiv 0$ for $m > S$. Note that in each case, (47) and (49) are quadratic forms in $\max\{M, S\}$ boundary nodes. These quadratic forms are not necessarily negative definite. However, the construction of the boundary conditions ensures that the energy decreases in typical cases (see Figure 8), resulting in a mostly, but not strictly monotonic decrease in energy.

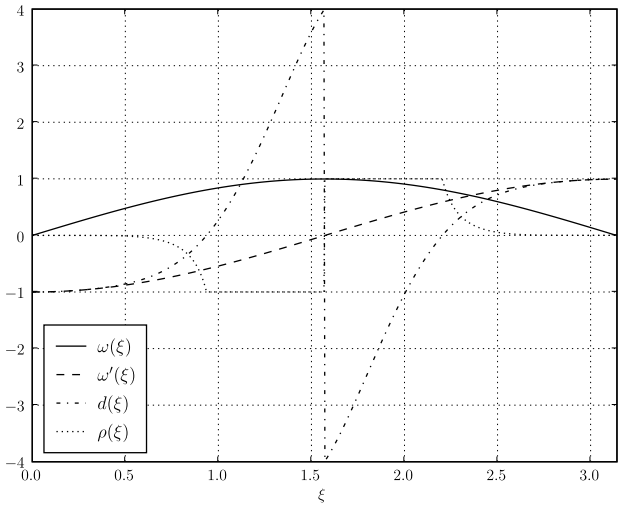

FIGURE 2. Dispersion relation $\omega(\xi)$, group velocity $\omega'(\xi)$, normalized energy dissipation rate $d(\xi)$, and relative dissipation rate error $\rho(\xi)$ for a Colonius-type boundary closure of order 5. Note that d and ρ are plotted for the left boundary for leftgoing waves and for the right boundary for rightgoing waves.

4.6. **Reflection coefficients.** A reflection coefficient at the boundary is commonly defined as follows. If, for a given frequency ω, there exist one leftgoing and one rightgoing normal mode (within a certain range of permissible frequencies), the approximate transparent boundary condition defines an amplitude ratio between the two modes at the boundary, the *reflection coefficient* [21].

For general nonreflecting boundary conditions as derived in this section, this construction becomes unwieldy, as there may be many incoming or outgoing modes with the same frequency ω. In principle, we could define a reflection matrix, but this would not yield a single scalar diagnostic quantity. Moreover, the dimension of this matrix depends on the shape of the dispersion curve which can be quite arbitrary and would have to be determined numerically using a global root finding method. We thus abandon the concept of reflection coefficient as a diagnostic tool and look instead at the error in the rate of energy dissipation as a function of lattice wave number ξ. The exact rate at which energy contained in wavenumber ξ leaves the domain of computation is proportional to the group velocity $\omega'(\xi)$, as can be seen by the following argument.

Fix $\xi \in [-\pi, \pi]$ such that it is not a critical point of the group velocity, let $N \gg 1$ be the largest resolved wave number (in the sense of the Fourier representation of the original advection equation), and let $t = N/\omega'(\xi)$ be the time when the phase in the Fourier integral (13) is stationary, i.e. when the wave packet with lattice wave number ξ leaves the domain of computation. (Recall that lattice wave numbers correspond to physical distance in the original advection problem, hence forming a

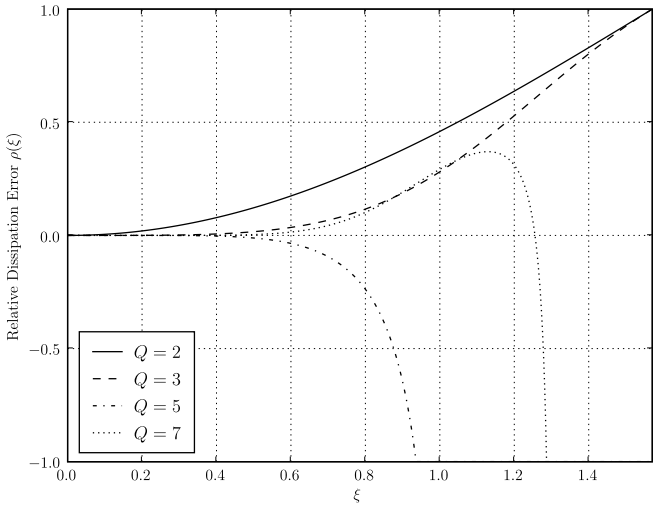

FIGURE 3. Relative dissipation rate error $\rho(\xi)$ for Colonius-type boundary closures of varying order Q. Qualitatively, ρ plays the role of a reflection coefficient.

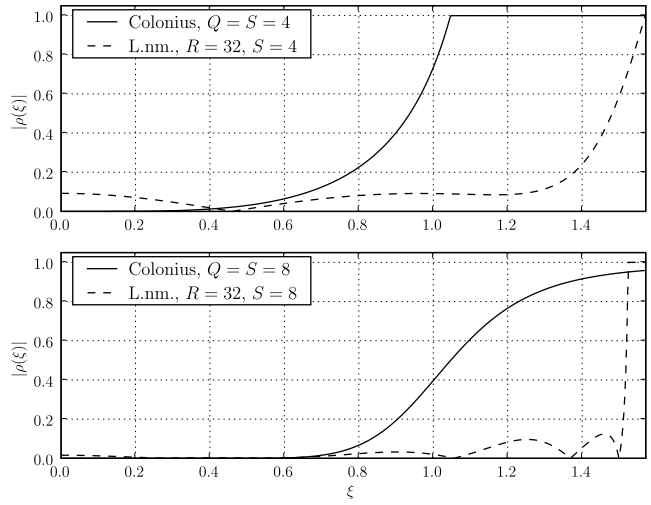

FIGURE 4. Comparison of the relative dissipation rate error $\rho(\xi)$ for a Colonius-type closure vs. a least-norm fit of an oversampled extrapolation.

continuum.) By the implicit function theorem,

$$\mathrm{d}t\,\omega'(\xi) + t\,\omega''(\xi)\,\mathrm{d}\xi = 0\,, \tag{50}$$

so that, by the Parseval identity,

$$\mathrm{d}E = \frac{1}{2\pi}\,|\theta(\xi,0)|^2\,\mathrm{d}\xi = -|\theta(\xi,0)|^2\,\frac{\omega'(\xi)}{2\pi\,t\,\omega''(\xi)}\,\mathrm{d}t \tag{51}$$

We recognize $1/\sqrt{2\pi t\omega''(\xi)}$ as the amplitude of the leading order contribution to the stationary phase asymptotics in (13). Thus, the energy of a wave packet with normalized amplitude leaves the computational domain with group velocity $\omega'(\xi)$.

Our approximate transparent boundary conditions have corresponding energy dissipation rates for normalized lattice waves on the right hand and left hand boundaries which read, according to (47) and (49), respectively,

$$d_{\mathrm{r}}(\xi) = 2\ \mathrm{Re}\sum_{m,n=S_0}^{S} \mathrm{e}^{\mathrm{i}\xi(n-m)} \sum_{l=S+1-n}^{M} c_l\,a_{n+l-S,m} \tag{52}$$

and

$$d_{\mathrm{l}}(\xi) = 2\ \mathrm{Re}\sum_{m,n=0}^{S_1} \mathrm{e}^{\mathrm{i}\xi(n-m)} \sum_{l=n}^{M} c_l\,a_{M+n-l,m}\,. \tag{53}$$

The error in the energy dissipation rate is therefore

$$\mathrm{d}E_{\mathrm{err}} = -|\theta(\xi,0)|^2\,\frac{\omega'(\xi)-d(\xi)}{2\pi\,t\,\omega''(\xi)}\,\mathrm{d}t = |\theta(\xi,0)|^2\,\frac{\omega'(\xi)-d(\xi)}{2\pi\,\omega'(\xi)}\,\mathrm{d}\xi \tag{54}$$

Motivated by this expression, we define a relative dissipation rate error function

$$\rho_{\mathrm{l,r}}(\xi) = \frac{\omega'(\xi)-d_{\mathrm{l,r}}(\xi)}{|\omega'(\xi)|+|d_{\mathrm{l,r}}(\xi)|}\,. \tag{55}$$

This function takes values between -1 and 1; it is zero if the wave with lattice wave number ξ passes the boundary unhindered. Thus, ρ can be seen as a generalized reflection coefficient.

5. Numerical tests for time-independent velocity

5.1. **Colonius-type closures.** We demonstrate the Colonius-type closures of Section 3 for $M = 1$. The velocity field is specified by $c_1 = 1$. This is the case to which the closed form solution of Appendix A applies.

Figure 2 shows the dispersion curve $\omega(\xi)$ on $[0,\pi]$; the behavior on $[-\pi,0]$ is symmetric to the window shown. Also shown are the corresponding group velocity $\omega'(\xi)$ and the actual energy dissipation rate $d(\xi)$. It is clearly seen that $d(\xi)$ approximates the group velocity very well near its extrema, but displays rapid, unphysical energy growth near the zeros of the group velocity. This behavior is reflected by the relative dissipation error rate.

Figure 3 shows how the dissipation rate error depends on order. Figure 4 compares Colonius-type closures with the least-norm oversampled method described in Section 4.3 with an equal-sized boundary stencil. The relative energy dissipation rate error of the least-norm computation is more uniformly distributed and, except for a small region near the zeros of the group velocity, does not exceed 10%.

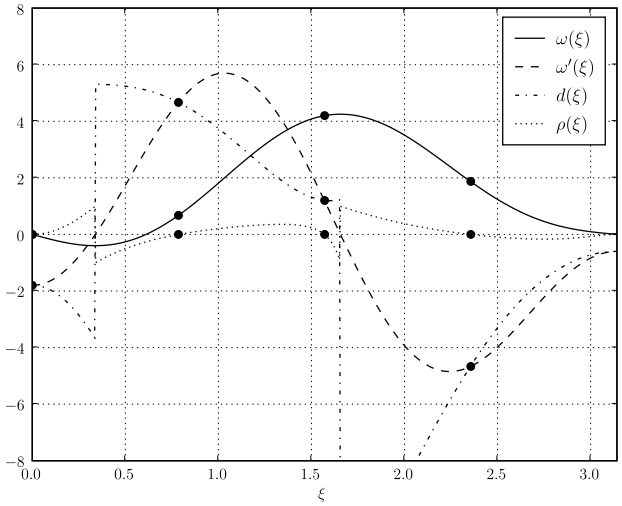

FIGURE 5. Dispersion relation $\omega(\xi)$, group velocity $\omega'(\xi)$, normalized energy dissipation rate $d(\xi)$, and relative dissipation rate error $\rho(\xi)$ for the equidistantly sampled boundary closure with $S^{\text{smpl}} = 8$ sample points.

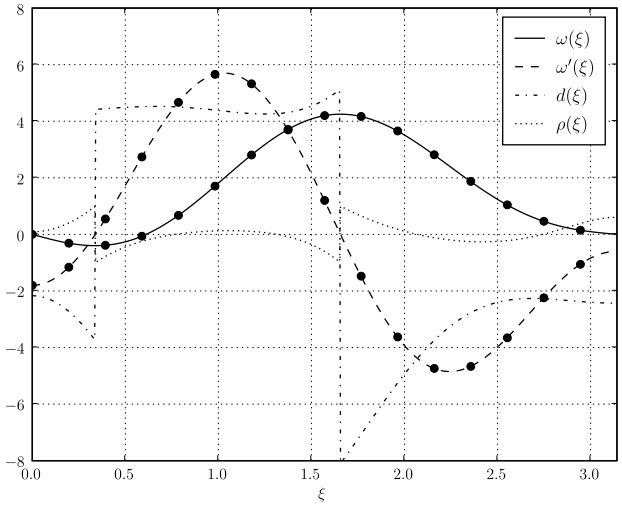

FIGURE 6. Dispersion relation $\omega(\xi)$, group velocity $\omega'(\xi)$, normalized energy dissipation rate $d(\xi)$, and relative dissipation rate error $\rho(\xi)$ for the equidistantly over-sampled boundary closure with $S^{\text{smpl}} = 32$ sample points and a boundary stencil of size $S = 4$ computed by a weighted least-norm fit.

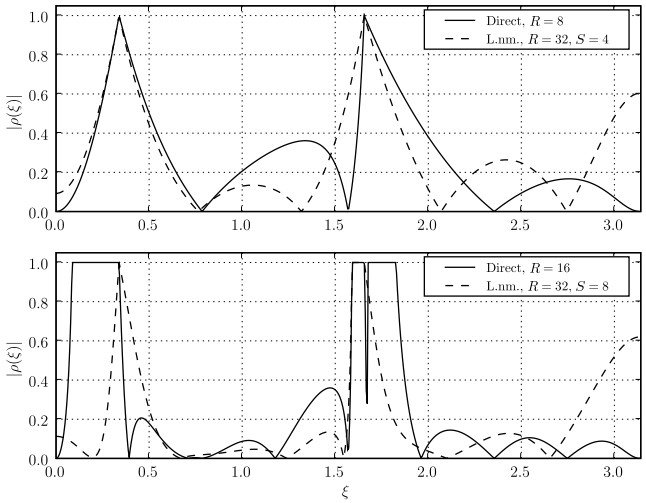

FIGURE 7. Comparison of the relative dissipation rate error $\rho(\xi)$ for a direct solution of the extrapolation equations vs. a least-norm fit of an oversampled extrapolation. Since the sample points are divided up between the left and the right boundary, a boundary stencil of size S corresponds to $S^{\text{smpl}} = 2S$ direct sample points.

5.2. **Equidistant closures.** The two equidistant closures, direct and least-norm, are evaluated on a test problem with $M = 3$ and $c_1 = 3$, $c_2 = -0.6$, $c_3 = -1.2$. The group velocity now has two maxima of different magnitude as well as two additional zeros.

Figure 5 shows the dispersion plot of direct equidistant sampling—sample points being indicated with bullets—and the resulting dissipation rate and error curves. The corresponding situation for the oversampled least-norm method with boundary stencils of equal size is shown in Figure 6. The qualitative difference between the two methods is marginal with the distribution of the error of the least-norm computation slightly more uniform. Thus, the biggest practical advantage of the least-norm computation is code simplification due to the predictable size of the boundary stencil—this point is moot in one, but significant in higher dimensions—and the time continuity of the boundary condition.

We compare a reference solution (computed on a grid five times larger) with a low order transparent boundary closure (for higher order closures some of the errors would be indiscernible in the plots) and with a brute-force Galerkin truncation. Figure 7 demonstrates that the quality of the boundary conditions depends mostly on the size of the stencil while there is no clear winner when comparing the direct solution technique with an oversampled least-norm solution. Thus, as mentioned before, the chief advantage of the least-norm solution is that it allows to specify stencil sizes *a priori*, and that it can guarantee continuity in time of the boundary conditions for nonstationary flows. Figure 7 also shows clearly that the approximate nonreflecting boundary conditions do worst for waves with near-vanishing group

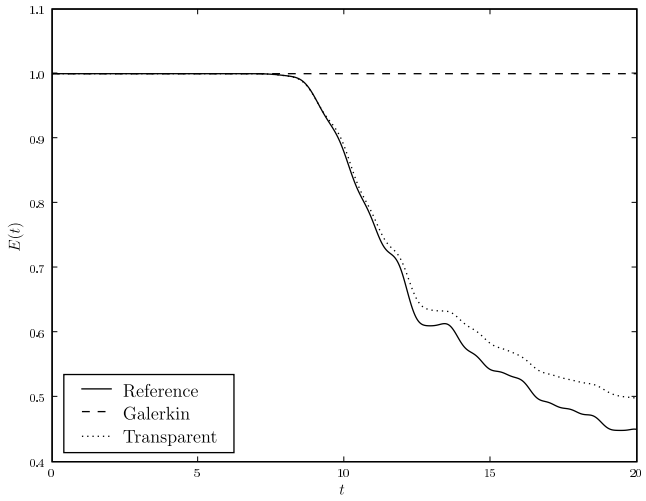

FIGURE 8. Time evolution of the energy for the solutions that correspond to the dispersion curve of Figure 5 and Figure 6. The initial data are concentrated on the zero mode. Shown are a reference computation on a much larger grid (solid line), a boundary closure with least-norm extrapolation and stencil size $S = 2$ (dotted line) and a Galerkin truncation (dashed line).

velocity. These, however, are the waves for which the *absolute* energy dissipation rate is very small.

Figure 8 shows that, while the Galerkin truncation does not dissipate energy, the transparent boundary conditions yield a qualitatively good approximation of the energy dissipation rate. Since the approximation error is mostly concentrated in the slow waves, the long-time error is worse than the behavior for short times.

Figure 9 gives time slices of the solutions on the Fourier grid. The large spurious reflections in the Galerkin case can be clearly seen. The fully two-dimensional field in physical space corresponding to the final time slice of Figure 9 is shown in Figure 10.

6. Time-dependent velocity fields

We generate an artificial time-dependent velocity field by letting its Fourier coefficients follow independent Ornstein–Uhlenbeck stochastic processes of the form

$$\mathrm{d}c(t) = -\alpha\, c(t)\,\mathrm{d}t + \sqrt{2\beta}\,\mathrm{d}W(t)\,, \tag{56}$$

where $W(t)$ is standard Brownian motion. This process admits a stationary Gaussian probability distribution which is controlled by only two parameters, the inverse correlation time α and the variance β/α; its time integral has a k^{-1} power spectrum. A more detailed description of the properties of the Ornstein–Uhlenbeck is given in Appendix B.

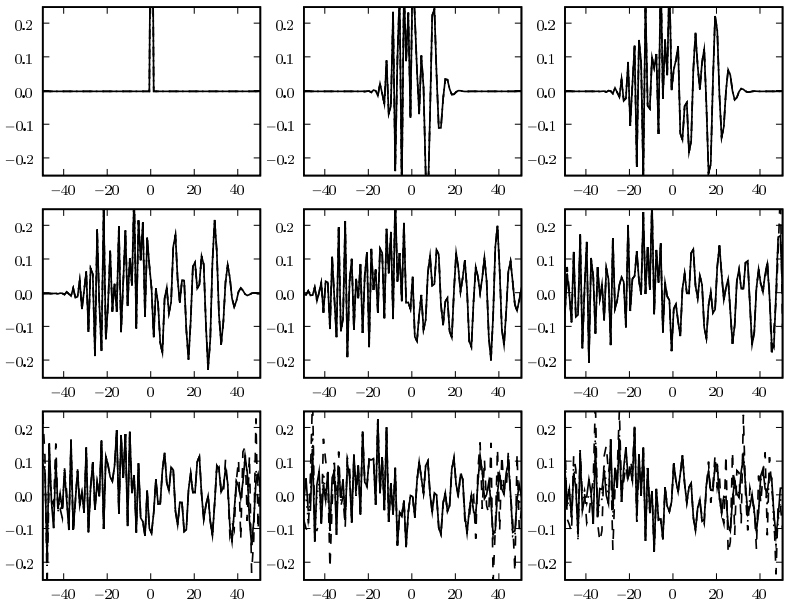

FIGURE 9. The evolution of the solution corresponding to the dispersion curve of Figure 5 and Figure 6 on the Fourier grid. The initial data are concentrated on the zero mode. Shown are a window into a reference solution computed on a much larger grid (solid line), a boundary closure with least-norm extrapolation and stencil size $S = 2$ (dotted line) and a Galerkin truncation (dashed line). The solution is shown at $t = 0, \frac{15}{8}, \ldots, \frac{15}{1}$.

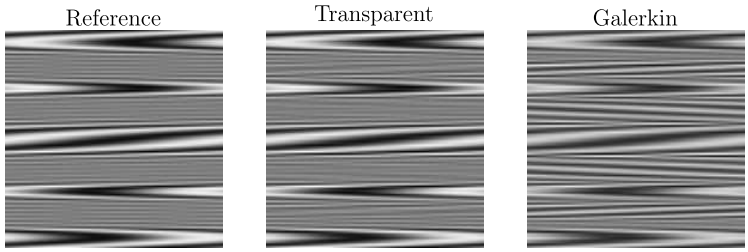

FIGURE 10. The solutions corresponding to the final time slice of Figure 9 in physical space.

We now reexamine the lattice ODE (8) under the assumption that the coefficients c_j depend on time. The normal mode solutions now take the more general form

$$\theta_l = \mathrm{e}^{\mathrm{i}\Omega(t)-\mathrm{i}\xi l}\,, \tag{57}$$

so that substitution into (8) gives

$$\omega(\xi,t) \equiv \dot\Omega(\xi,t) = -\mathrm{i}\sum_{j=-M}^{M} c_j(t)\,\mathrm{e}^{\mathrm{i}j\xi}\,. \tag{58}$$

Integration yields the dispersion relation

$$\Omega(\xi,t) = -\mathrm{i}\sum_{j=-M}^{M} C_j(t)\,\mathrm{e}^{\mathrm{i}j\xi} \qquad \text{with} \qquad C_j(t) = \int_0^t c_j(t)\,\mathrm{d}t\,. \tag{59}$$

The general solution to (8) is given by the Fourier integral

$$\theta_l(t) = \frac{1}{2\pi}\int_{-\pi}^{\pi} \mathrm{e}^{\mathrm{i}\Omega(\xi,t)-\mathrm{i}l\xi}\,\theta(\xi,0)\,\mathrm{d}\xi\,. \tag{60}$$

For large l, the exponential oscillates rapidly unless

$$\frac{\mathrm{d}}{\mathrm{d}\xi}\big(\Omega(\xi,t)-l\xi\big) = 0\,. \tag{61}$$

Thus, ideal transparent boundary conditions at a wave number $N \gg 0$ behave asymptotically as follows. A wave packet with wave number ξ will remain in the domain of computation until it reaches the boundary, i.e. if the corresponding phase in (60) becomes stationary at the boundary. The packet is then absorbed by the boundary and will not re-enter the domain of computation. In particular, the mean time for a wave packet to remain in the domain is the mean exit time of the random variable $\mathrm{d}\Omega/\mathrm{d}\xi$ from the domain $[-N,N]$.

If the coefficients c_j of the velocity field follow Ornstein–Uhlenbeck processes with identical parameters, then Ω as well as $\mathrm{d}\Omega/\mathrm{d}\xi$ are the time integrals or *displacements* of an Ornstein–Uhlenbeck process whose parameters are determined as follows. The coefficient process (58) can be written, using the symmetry (10),

$$\omega(\xi,t) = -\mathrm{i}\sum_{j=1}^{M}\big(c_j\,\mathrm{e}^{\mathrm{i}j\xi} - \overline{c}_j\,\mathrm{e}^{-\mathrm{i}j\xi}\big) = 2\sum_{j=1}^{M}\big(b_j(t)\,\cos j\xi + a_j(t)\,\sin j\xi\big)\,, \tag{62}$$

where $c_j \equiv a_j + \mathrm{i}b_j$, and therefore

$$\frac{\mathrm{d}\omega}{\mathrm{d}\xi} = 2\sum_{j=1}^{M} j\big(a_j(t)\,\cos j\xi - b_j(t)\,\sin j\xi\big)\,. \tag{63}$$

According to Lemma 5, for fixed j the process $a_j(t)\,\cos j\xi - b_j(t)\,\sin j\xi$ is also distributed according to an Ornstein–Uhlenbeck process driven by white noise with variance parameter β, and $\mathrm{d}\omega/\mathrm{d}\xi$ follows an Ornstein–Uhlenbeck process driven by white noise with variance parameter

$$\beta_M \equiv \beta\sum_{j=1}^{M}(2j)^2 = \tfrac{2}{3}\,\beta\,M\,(M+1)\,(2M+1)\,. \tag{64}$$

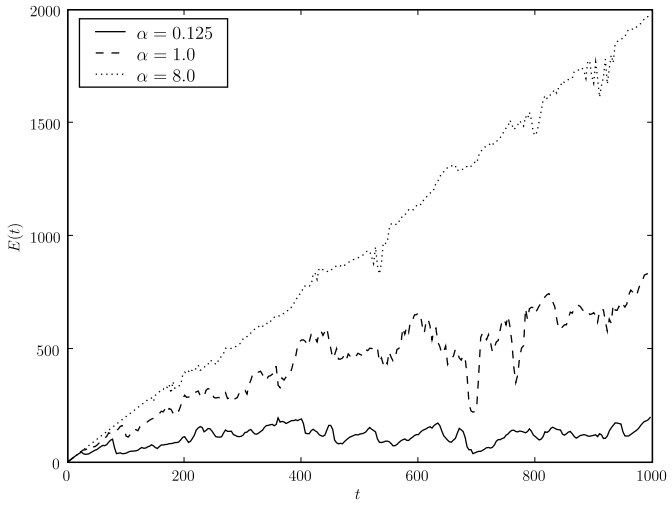

FIGURE 11. Evolution of total energy for the shear flow forced by the stochastic process of Section 6 on the Fourier lattice of size $N = 100$. The energies are obtained by using a transparent closure at $N = 200$, then truncating to the smaller $N = 100$ grid.

According to Hagan, Doering, and Levermore [13], the mean exit time is given by

$$\begin{aligned}\mathbb{E}[T_{\mathrm{ex}}] &= \frac{1}{2}\,\frac{\alpha^2}{\beta_M}\left(N - \frac{\beta_M^{1/2}}{\alpha^{3/2}}\,\zeta(\tfrac{1}{2})\right)^2 - \frac{1}{2\alpha}\,\operatorname{Var}\left[\frac{\mathrm{d}\omega}{\mathrm{d}\xi}(0)\right] + \frac{1}{\alpha}\,\kappa \\ &= \frac{1}{2}\,\frac{\alpha^2}{\beta_M}\left(N - \frac{\beta_M^{1/2}}{\alpha^{3/2}}\,\zeta(\tfrac{1}{2})\right)^2 - \frac{1}{2}\,\frac{\beta_M}{\alpha^2} + \frac{1}{\alpha}\,\kappa\,, \end{aligned} \tag{65}$$

where ζ is the Riemann zeta function so that $-\zeta(\frac{1}{2}) = 1.4603545\ldots$ and $\kappa = 0.2274981\ldots$ is another numerical constant, up to exponentially small errors in

$$r \equiv N\,\alpha\,\sqrt{\frac{\alpha}{\beta_M}}\,. \tag{66}$$

Since β_M/α is the variance of the group velocity process $\mathrm{d}\omega/\mathrm{d}\xi$, the limit $r \gg 1$ is the regime where the size of the lattice domain is much larger than the typical distance a wave travels on the correlation time scale $1/\alpha$. Also note that the parameters of [13] are identified with our notation via

$$\varepsilon_{\mathrm{HDL}} = \frac{1}{\sqrt{\alpha}} \qquad \text{and} \qquad \sigma_{\mathrm{HDL}} = \frac{\sqrt{\beta_M}}{\alpha}\,. \tag{67}$$

7. Numerical tests for time-dependent velocity

We now test out the transparent boundary conditions with a time dependent velocity field which is generated, as described in the previous section, by having the Fourier coefficients follow independent Ornstein–Uhlenbeck processes.

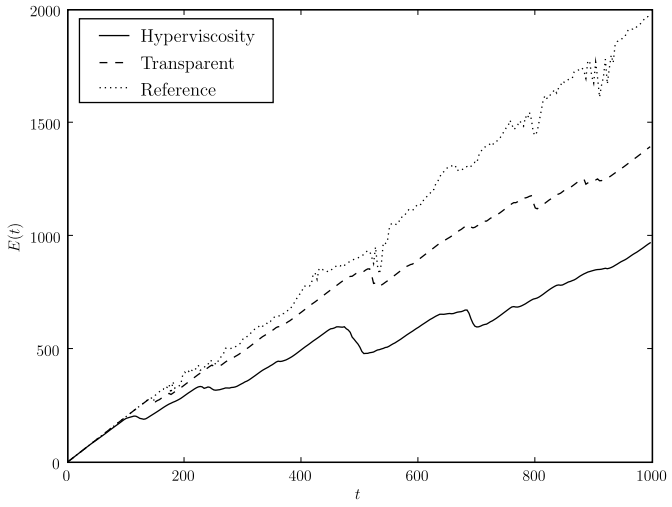

FIGURE 12. Evolution of total energy for the shear flow forced by the stochastic process of Section 6 with $\alpha = 8$. This graph compares the reference computation of Figure 11 with a transparent closure and a Galerkin truncated simulation with hyperdiffusion of order 8 and $\nu = 10^{-16}$

We are interested in the time-averaged energy spectrum in a statistical steady-state. Thus, we must consider a forced-dissipative setting where the forcing is confined to low wavenumbers and dissipation arises exclusively through passage of wave packets through the nonreflecting boundary. We force the system such that the energy flux is kept constant. In our implementation the forcing function is a multiple of the modes $|k| \leq S^{\mathrm{drv}}$ where the radius of the driving stencil S^{drv} is small; here $S^{\mathrm{drv}} = 1$. The constant of proportionality is adjusted to keep the rate of energy injection constant. (A fixed forcing function whose amplitude is adjusted leads to small denominators and subsequent stability problems.)

Since the right hand side of the differential equation is not differentiable in time, we do not need high order in the time integrator. Moreover, standard time stepping control will fail on this type of data. On the other hand, we need an i-stable scheme—an integrator whose stability region includes part of the imaginary axis. We thus settle for the standard fourth order Runge–Kutta scheme where the time step is determined by the CFL condition of the advection problem. Moreover, we discretize the stochastic process such that it is constant throughout a full Runge–Kutta time step. This ensures that at least the energy balance is accurate to order four, even though the full trajectory error cannot be better than order one. If the Ornstein–Uhlenbeck process is not frozen throughout the time step, we see significant energy drift even in situations where no energy is passing through the boundary.

In our test we fix $M = 3$, the variance of the Ornstein–Uhlenbeck processes to be 1 so that $\beta = 1/\alpha$, compute the boundary operators using least-norm equidistant

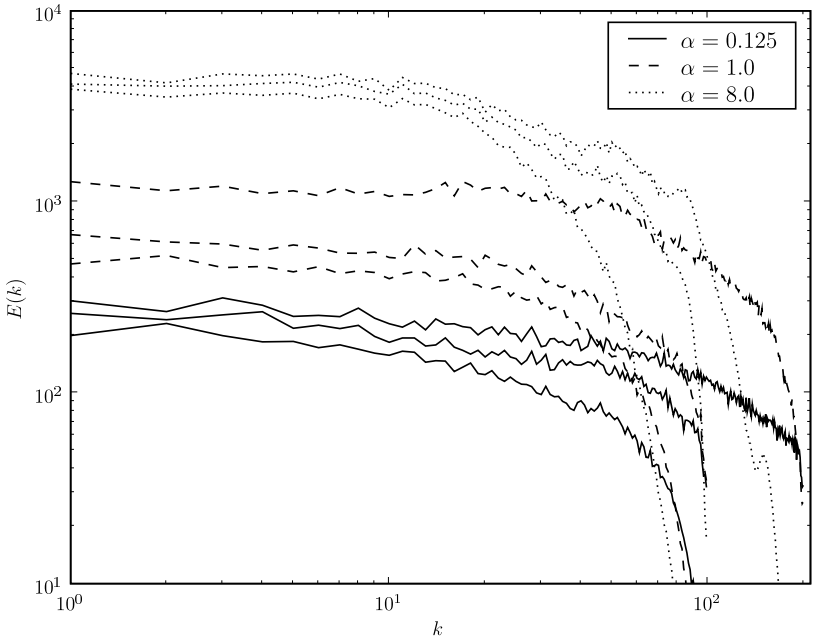

FIGURE 13. The time-averaged energy spectra corresponding to Figures 11 and 12. In each triple of curves with same α, the upper curve belongs to the "Reference" computation with transparent boundary closure on a Fourier lattice of size $N = 200$, the middle curve to a transparent boundary closure at $N = 100$, and the bottom curve a Galerkin truncation with hyperdiffusion of order 8 and $\nu = 10^{-16}$.

oversampling with $S^{\text{smpl}} = 20$ sampling points, and use a boundary stencil of size $S = 4$ and the rate of energy influx equal to 1 where only the modes with wavenumbers $k = -1, 0, 1$ are forced.

Figure 11 shows the evolution of the total energy on a Fourier lattice of size $N = 100$ for varying time constant α. The effect of a transparent closure vs. a Galerkin truncation with hyperdiffusion is seen in Figure 12. The diffusion coefficient was chosen as small as possible, namely, such that a pile-up of energy at the cut-off is barely visible (and remains outside of the window shown). The energy spectra corresponding to various combinations of method and parameter α are shown in Figure 13.

We identify three different regimes. When α is small, corresponding to $r \ll 1$, the rate of change of velocity is slow compared to the group velocity of most lattice waves, and the system behaves almost like with a static velocity field. When α is large, corresponding to $r \gg 1$, the diffusion of energy to high wave numbers is slow and energy is piling up in the low modes; the transparent boundary conditions are not exercised significantly. In the intermediate regime, we see that the transparent boundary conditions are significantly more dissipative on the smaller Fourier lattice,

because with high probability the group velocity of wave packets which have left the smaller Fourier lattice will change such that they return to it. A transparent boundary condition, however, will simply dissipate the wave packet at its first passage time.

8. Concluding remarks

In this paper, we have investigated transparent boundary conditions in spectral space for the numerical simulation of passive-tracer advection by a one-dimensional shear flow. The boundary condition is based on the assumption that the shear flow has compact spectral support. We formulated an asymptotic boundary closure scheme that exploits a small parameter, namely, the size of the spectral support of the shear flow divided by the spectral truncation of the numerical scheme. This brings the numerical problem into a form that can be analyzed based on a dispersion relation for waves in spectral space, and the boundary condition in spectral space can then be formulated based on a group-velocity decomposition into outgoing and incoming waves in spectral space. In physical space, the dispersion relation is proportional to the shear flow profile and these waves correspond to the singular neutral modes that form the continuous spectrum of the original shear flow. Several different boundary schemes were formulated and tested based on different sampling strategies from the underlying dispersion relation.

For steady shear flows the performance of the transparent boundary condition in spectral space was tested successfully against simple exact solutions and against alternative numerical approaches such as the standard Galerkin truncation. Here the scheme performed very well. For randomly fluctuating shear flows the performance of the scheme was dependent on the ratio between the timescale of the flow fluctuations and the straining rate; a somewhat less clear result emerged from the simulations in these scenarios. Finally, we have begun to investigate the two-dimensional version of this scheme. Here the straight streamlines of the shear flow are replaced by the curved streamlines of an incompressible two-dimensional flow and the analysis in spectral space is significantly complicated by the rotation of advected tracer structures along the curved streamlines. We hope to report on this on-going project in the future.

Appendix A. Exact solution for sinusoidal velocity fields

When the velocity field contains only a single wave number, so that, without loss of generality,

$$u(y) = -\sin(y)\,, \tag{68}$$

the closure problem can be solved explicitly. However, if more than one wave number pair is active, explicit formulas of this type do not appear to be available and we have to resort to approximately nonreflecting boundary closures. In the following, we state the one-mode solution as a benchmark and illustration of the more general procedure.

For u as in above,

$$u_1 = -\frac{1}{2\mathrm{i}}\,, \qquad u_{-1} = \frac{1}{2\mathrm{i}}\,, \qquad \text{and} \qquad u_l = 0 \text{ for all } j \neq \pm 1\,. \tag{69}$$

Plugging (69) into (6), we obtain

$$\partial_t \theta_{kl} - \frac{k}{2}\,\theta_{k,l-1} + \frac{k}{2}\,\theta_{k,l+1} = 0\,. \tag{70}$$

Since the equation is linear in θ, it is sufficient to consider the evolution of one particular horizontal wavenumber, $k = 1$, say. Different k can be achieved by rescaling time; more general functions in x are treated by superposition. Dropping the horizontal wave number index for notational simplicity, we arrive at a system of coupled ODEs,

$$\dot\theta_l = \tfrac{1}{2}\,\theta_{l-1} - \tfrac{1}{2}\,\theta_{l+1}\,. \tag{71}$$

We seek a solution in terms of the generating function

$$\phi(t;\varepsilon) = \sum_{l\in\mathbb{Z}} \theta_l(t)\,\varepsilon^l\,, \tag{72}$$

which is a formal power series in the artificial parameter ε. Equation (71) implies that

$$\dot\phi = \tfrac{1}{2}\,\varepsilon^{-1}\,\phi - \tfrac{1}{2}\,\varepsilon\,\phi\,, \tag{73}$$

so that

$$\phi(t;\varepsilon) = \phi(0;\varepsilon)\,\mathrm{e}^{\frac{1}{2}(\varepsilon-1/\varepsilon)t}\,. \tag{74}$$

The exponential factor is recognized as the generating function of the Bessel functions of the first kind [2, 9.1.41],

$$\mathrm{e}^{\frac{1}{2}(\varepsilon-1/\varepsilon)t} = \sum_{l\in\mathbb{Z}} J_l(t)\,\varepsilon^l\,, \tag{75}$$

so that, if the profile is initially vertically homogeneous, i.e., $\phi(0;\varepsilon) = 1$,

$$\theta_l(t) = J_l(t)\,. \tag{76}$$

More generally, if

$$\phi(0;\varepsilon) = \sum_{l\in\mathbb{Z}} \theta_l(0)\,\varepsilon^l\,, \tag{77}$$

we find that

$$\theta_l(t) = \sum_{n+m=l} \theta_n(0)\,J_m(t)\,. \tag{78}$$

Appendix B. Ornstein–Uhlenbeck process

In this appendix, we review some elementary properties of the Ornstein–Uhlenbeck process for the benefit of the reader and also to fix notation and scalings. This is essentially textbook material and can, for example, be found in [8].

Lemma 1. *The Ornstein–Uhlenbeck process has the explicit solution*

$$c(t+s) = \mathrm{e}^{-\alpha s}\,c(t) + \sqrt{2\beta}\int_t^{t+s} \mathrm{e}^{\alpha(s-r)}\,\mathrm{d}W(t+r)\,. \tag{79}$$

In particular,

$$\mathbb{E}[c(t+s)] = \mathrm{e}^{-\alpha s}\,\mathbb{E}[c(t)]\,. \tag{80}$$

Proof. Without loss of generality, we take $s = 0$ and define

$$C(t) = \int_0^t c(r)\,\mathrm{d}r\,. \tag{81}$$

(Since c is continuous, this is a classical integral.) Then the integral version of the Ornstein–Uhlenbeck SDE (56) reads

$$\dot{C}(t) = c(0) - \alpha\,C(t) + \sqrt{2\beta}\,W(t)\,. \tag{82}$$

We multiply with an integrating factor, so that

$$\mathrm{e}^{\alpha t}\,c(t) + \alpha\,\mathrm{e}^{\alpha t}\,C(t) = \mathrm{e}^{\alpha t}\,c(0) + \sqrt{2\beta}\,\mathrm{e}^{\alpha t}\,W(t)\,, \tag{83}$$

then integrate and multiply by α,

$$\alpha\,\mathrm{e}^{\alpha t}\,C(t) = c(0)\,(\mathrm{e}^{\alpha t} - 1) + \alpha\,\sqrt{2\beta}\int_0^t \mathrm{e}^{\alpha r}\,W(r)\,\mathrm{d}r\,. \tag{84}$$

Noting that the Itô formula implies the integration by parts identity

$$\int_0^t \mathrm{e}^{\alpha r}\,\mathrm{d}W(r) = \mathrm{e}^{\alpha t}\,W(t) - \alpha\int_0^t \mathrm{e}^{\alpha r}\,W(r)\,\mathrm{d}r\,, \tag{85}$$

we find, by subtracting (84) from (83), that

$$\mathrm{e}^{\alpha t}\,c(t) = c(0) + \sqrt{2\beta}\int_0^t \mathrm{e}^{\alpha r}\,\mathrm{d}W(r)\,. \tag{86}$$

This identity is directly equivalent to that stated in the lemma. □

Lemma 2. *If $c(t)$ is a random variable which evolves according to the Ornstein–Uhlenbeck process* (56)*, then*

$$\mathbb{E}[c^2(t)] = \mathrm{e}^{-2\alpha t}\,\mathbb{E}[c^2(0)] + \frac{\beta}{\alpha}\,(1 - \mathrm{e}^{-2\alpha t})\,. \tag{87}$$

Proof. By the Itô formula,

$$c^2(t) - c^2(0) = \int_0^t \big(-2\alpha\,c^2(r) + 2\beta\big)\,\mathrm{d}t + 2\sqrt{2\beta}\int_0^t c(r)\,\mathrm{d}W(r)\,. \tag{88}$$

Taking the expectation, noting that $a(r)$ and the increments $\mathrm{d}W(r)$ are independent, we obtain

$$\mathbb{E}[c^2(t)] - \mathbb{E}[c^2(0)] = -2\alpha\int_0^t \mathbb{E}[c^2(r)]\,\mathrm{d}r + 2\beta t\,. \tag{89}$$

This is easily written as an ODE in $\mathbb{E}[c^2(t)]$ and readily solved. □

Corollary 3. *The co-variance of the Ornstein–Uhlenbeck process satisfies*

$$\mathrm{Cov}[c(t), c(t+s)] = \mathrm{Var}[c(0)]\,\mathrm{e}^{-\alpha(2t+s)} + \frac{\beta}{\alpha}\,(1 - \mathrm{e}^{-2\alpha t})\,\mathrm{e}^{-\alpha s}\,, \tag{90}$$

$$\mathrm{Cov}[c(t), c(t+s) \mid c(0) = \gamma] = \frac{\beta}{\alpha}\,(1 - \mathrm{e}^{-2\alpha t})\,\mathrm{e}^{-\alpha s}\,, \tag{91}$$

and in the stationary case,

$$\mathrm{Cov}[c(t), c(t+s)] = \frac{\beta}{\alpha}\,\mathrm{e}^{-\alpha s}\,. \tag{92}$$

Proof. Use Lemma 1 to express $c(t+s)$ in terms of $c(t)$ and note that $c(t)$ and

$$\int_t^{t+s} \mathrm{e}^{\alpha(s-r)}\,\mathrm{d}W(t+r) \tag{93}$$

are independent random variables, so that

$$\begin{aligned}\mathrm{Cov}[c(t),c(t+s)] &= \mathbb{E}[c(t)\,c(t+s)] - \mathbb{E}[c(t)]\,\mathbb{E}[c(t+s)] \\ &= \mathbb{E}[c^2(t)]\,\mathrm{e}^{-\alpha s} - \mathbb{E}[c(t)]^2\,\mathrm{e}^{-\alpha s}\end{aligned} \tag{94}$$

The first identity follows by (80), the other two are direct consequences. □

Corollary 4. *A discrete-time sample time series for the Ornstein–Uhlenbeck process is given by*

$$c(t+\Delta t) = c(t)\,\mathrm{e}^{-\alpha\Delta t} + N(0,\sigma)\,, \tag{95}$$

where $N(0,\sigma)$ is a normally distributed random variable with mean 0 and variance

$$\sigma^2 = \frac{\beta}{\alpha}\,(1-\mathrm{e}^{-2\alpha\Delta t})\,. \tag{96}$$

Proof. Lemma 1 shows that the increments are Gaussian with zero mean. Their variance is explicitly given by (91). This fully characterizes the discrete time sample process. □

Lemma 5. *If $a(t)$ and $b(t)$ are Ornstein–Uhlenbeck processes with identical correlation time $1/\alpha$ and variance 2β, then $c(t) = \sigma\,a(t) + \rho\,b(t)$ follows an Ornstein–Uhlenbeck process with correlation time $1/\alpha$ and variance $2\beta(\sigma^2+\rho^2)$.*

Proof. By definition, $c(t)$ follows the integral form of the SDE

$$c(t) - c(0) = -\alpha\int_0^t c(s)\,\mathrm{d}s + \sqrt{2\beta}\,\big(\sigma\,W_1(t) + \rho\,W_2(t)\big)\,, \tag{97}$$

where $W_1 \sim N(0,t)$ and $W_2 \sim N(0,t)$ are independent Wiener processes. Hence, $\sigma\,W_1(t) + \rho\,W_2(t) \sim N(0,(\sigma^2+\rho^2)t) \sim \sqrt{\sigma^2+\rho^2}\,N(0,t)$. Thus, $c(t)$ is distributed according to

$$\mathrm{d}c(t) = -\alpha\,c(t)\,\mathrm{d}t + \sqrt{2\beta(\sigma^2+\rho^2)}\,\mathrm{d}W(t)\,, \tag{98}$$

where $W(t)$ is standard Brownian motion. □

Acknowledgments

This work was performed while MO was visiting the Courant Institute of Mathematical Sciences supported by a Max–Kade Fellowship.

References

[1] M. Martins Afonso, A. Celani, R. Festa, and A. Mazzino, *Large-eddy-simulation closures of passive scalar turbulence: a systematic approach*, J. Fluid Mech. **496** (2003), 355–364.
[2] M. Abramowitz and I.A. Stegun, "Handbook of Mathematical Functions," United States National Bureau of Standards Applied Mathematics Series, Vol. 55, 1964.
[3] L. Brillouin, "Wave Propagation in Periodic Structures," Dover, New York, 1953.
[4] L. Brillouin, "Wave Propagation and Group Velocity," Academic Press, New York, 1960.
[5] T. Colonius, *Numerically nonreflecting boundary and interface conditions for compressible flow and aero-acoustic computations*, AIAA J. **35** (1997), 1126–1133.
[6] T. Colonius and H. Ran, *A super-grid-scale model for simulating compressible flow on unbounded domains*, J. Comput. Phys. **182** (2002), 191–212.
[7] T. Dombre, U. Frisch, J.M. Greene, M. Hénon, A. Mehr, and A. Soward, *Chaotic streamlines in the ABC flows*, J. Fluid Mech. **167** (1986), 353–391.

[8] J.L. Doob, "Stochastic processes", Wiley, New York, 1953.
[9] J. Frank and S. Reich, *Energy-conserving semi-discretizations and spurious numerical reflections*, preprint.
[10] M.J. Grote and J.B. Keller, *Exact nonreflecting boundary conditions for the time dependent wave equation*, SIAM J. Appl. Math. **55** (1995), 280–297.
[11] P.H. Haynes and J. Anglade, *The vertical-scale cascade of atmospheric tracers due to large-scale differential advection*, J. Atmos. Sci. **54** (1997), 1121–1136.
[12] J.B. Keller and D. Givoli, *Exact non-reflecting boundary conditions*, J. Comput. Phys. **82** (1989), 172–192.
[13] P.S. Hagan, C.R. Doering, and C.D. Levermore, *Mean exit times for particles driven by weakly colored noise*, SIAM J. Appl. Math. **49** (1989), 1480–1513.
[14] C. Meneveau and J. Katz, *Scale-invariance and turbulence models for large-eddy simulation*, Annu. Rev. Fluid Mech. **32** (2000), 1–32.
[15] C.W. Rowley and T. Colonius, *Discretely nonreflecting boundary conditions for linear hyperbolic systems*, J. Comput. Phys. **157** (2000), 500–538.
[16] R. Salmon, "Lectures on Geophysical Fluid Dynamics", Oxford University Press, Oxford, 1998.
[17] K.S. Smith, *Comments on "The k^{-3} and $k^{-5/3}$ energy spectrum of atmospheric turbulence: Quasigeostrophic two-level model simulation"*, J. Atmos. Sci. **61** (2004), 937–941.
[18] L.N. Trefethen, *Group velocity in finite difference schemes*, SIAM Rev. **24** (1982), 113–136.
[19] K.K. Tung and W.W. Orlando, *The k^{-3} and $k^{-5/3}$ energy spectrum of atmospheric turbulence: Quasigeostrophic two-level model simulation*, J. Atmos. Sci. **60** (2003), 824–835.
[20] R. Vichnevetsky and B. Peiffer, *Error waves in finite element and finite difference methods for hyperbolic equations*, in: Advances in Computer Methods for Partial Differential Equations, Pub. AICA, 1975.
[21] R. Vichnevetsky, E. Sciubba, and Y. Pak, *Numerical upstream boundary conditions that reduce spurious reflections*, in Advances in Computer Methods for Partial Differential Equations IV, Pub. IMACS, 1981.
[22] R. Vichnevetsky, *Wave propagation analysis of difference schemes for hyperbolic equations: A review*, Int. J. Numer. Methods Fluids **7** (1987), 409–452.

E-mail address, M. Oliver: `oliver@member.ams.org`

(M. Oliver) School of Engineering and Science, Jacobs University Bremen, 28759 Bremen, Germany

E-mail address, O. Bühler: `obuhler@cims.nyu.edu`

(O. Bühler) Courant Institute of Mathematical Sciences, New York University, New York, NY 10012, USA